Noname manuscript No. (will be inserted by the editor)

- Analytical model coupling Ekman and surface layer structure in atmospheric boundary layer flows
- Ghanesh Narasimhan · Dennice F.
- 4 Gayme · Charles Meneveau
- 6 Received: DD Month YEAR / Accepted: DD Month YEAR

7 Abstract

We introduce an analytical model that describes the vertical structure of Ekman boundary layer flows coupled to the MOST surface layer representation, which is valid for conventionally neutral (CNBL) and stable (SBL) atmospheric 10 conditions. The model is based on a self-similar profile of horizontal stress for 11 both CNBL and SBL flows that merges the classic 3/2 power law profile with 12 a MOST-consistent stress profile in the surface layer. The velocity profiles are 13 then obtained from the Ekman momentum balance equation. The same stress 14 model is used to derive a new self-consistent Geostrophic Drag Law (GDL). We determine the ABL height h using an equilibrium boundary layer height 16 model and parameterize the surface heat flux for quasi-steady SBL flows as 17 a function of a prescribed surface temperature cooling rate. The ABL height 18 and GDL equations can then be solved together to obtain the friction velocity 19 (u_*) and the cross-isobaric angle (α_0) as a function of known input parameters such as the Geostrophic wind speed and surface roughness z_0 . We show 21 that the model predictions agree well with predictions from the literature and 22 newly generated Large Eddy Simulations (LES). These results indicate that the proposed model provides an efficient and relatively accurate self-consistent 24 approach for predicting the mean wind velocity distribution in CNBL and SBL 25 flows.

Keywords Atmospheric boundary layer · Geostrophic drag law · Large eddy
 simulation

Ghanesh Narasimhan ghanesh91@gmail.com

Dennice F. Gayme dennice@jhu.edu

Charles Meneveau meneveau@jhu.edu

50

51

52

53

55

56

57

59

60

61

62

63

64

65

66

67

69

70

71

1 Introduction

The atmospheric boundary layer (ABL) refers to the lower part of the at-30 mosphere, which interacts with processes on the Earth's surface, involving 31 exchanges of heat, moisture, and momentum. In this region, Coriolis and fric-32 tional forces influence the vertical variation of the wind. The resulting wind 33 veers across heights leading to an Ekman-like spiral (Ekman, 1905). Under-34 standing the wind veering under realistic atmospheric conditions is essential for 35 applications such as wind energy, pollutant transport modeling, and boundary layer parameterizations for climate models. An example of this importance is 37 highlighted in a study by Walcek (2002), which demonstrated that the pres-38 ence of an Ekman spiral flow leads to a skewed structure in pollution puffs, challenging the traditional assumption of a simple shape for pollutant plumes. Wind veering in the ABL has similarly been shown to change the shape of 41 wind turbine wake regions to be more sheared in the lateral direction, (e.g., 42 Abkar et al. (2018) and Narasimhan et al. (2022)), versus the symmetric wakes 43 assumed when neglecting the effect of veer. This lateral extension of the wake due to wind veer can significantly impact the performance of downstream tur-45 bines. These and other findings underscore the importance of accounting for 46 properties of ABL that influence wind farm flow physics and pollutant trans-47

A number of studies have addressed the classical problem of modeling wind velocity distributions in the ABL. These velocities are typically obtained by solving the steady-state Ekman mean momentum equations. The traditional approach to solving these equations involves invoking the Boussinesq eddyviscosity hypothesis to model turbulent shear stresses. Ekman (1905) solved these equations assuming a constant eddy-viscosity and obtained the classical solution involving a spiraling flow velocity profile based on trigonometric and exponential functions. However, in the turbulent ABL, the eddy-viscosity actually varies with height. In particular, the atmospheric surface layer (ASL), located close to the surface, exhibits a linear dependence of eddy-viscosity with height, assuming that the mixing length varies linearly with distance to the ground (Tennekes and Lumley, 1972). This layer, in which the constant turbulent shear stress is proportional to the square of the friction velocity (u_*) , is often referred to as the constant flux layer (Horst, 1997; Wyngaard, 2010). Within the ASL, wind veering is negligible, and the streamwise velocity follows a logarithmic profile (if the effects of thermal stratification are neglected).

Above the ASL lies the Ekman layer, which has flow scales that are large enough to be influenced by Coriolis effects leading to wind veering. Here, the logarithmic velocity profile that is valid in the ASL does not satisfy the Geostrophic wind condition approaching the top boundary. Ellison (1955) addressed this issue by solving the Ekman momentum equations with a linearly varying eddy-viscosity throughout the layer and obtained analytical solutions for velocities involving Kelvin or modified Bessel functions (Krishna, 1980; Kelly and van der Laan, 2023). These analytical relations show that solutions depend on z/h_e , where $h_e = u_*/f_c$ (Rossby and Montgomery, 1935) and

 f_c is the Coriolis parameter. However, the assumption of linearly increasing eddy-viscosity in Ellison (1955) is inaccurate outside of the surface layer. Instead the eddy-viscosity decays as it approaches the Geostrophic region, where turbulent stresses are negligible. Blackadar (1962) addressed this problem by invoking Prandtl's mixing length theory to propose an eddy-viscosity profile that increases linearly within the ASL and decays within the Ekman layer. Blackadar (1962) solved the associated equations numerically to obtain ABL velocities that exhibit a logarithmic profile within the ASL and form an Ekman spiral structure further away from the surface, eventually merging with the Geostrophic wind. However, the form of these equations did not allow for analytical solutions.

In a recent study, Constantin and Johnson (2019) showed that Ekman's mean momentum equations predict a spiraling velocity profile for any assumed form of eddy-viscosity that is bounded and reaches a constant value at larger heights. They explicitly showed that assuming a linearly varying eddy-viscosity closer to the surface and a constant value at greater heights leads to Bessel-type solutions for the mean velocity components. Similarly, assuming exponential eddy-viscosity variation closer to the surface that tends to a constant further above results in solutions given by hypergeometric functions. Although these explicit analytical solutions are instructive, evaluating such special functions becomes cumbersome and the complexity is often similar to having to solve the eddy-viscosity momentum (1D ordinary differential) equations numerically.

The effects of ground temperature add to the challenges of analytically describing the velocity profile in the ABL. Heating of the ground leads to the formation of an unstable Convective Boundary Layer (CBL), while cooling the ground results in a Stable Atmospheric Boundary Layer (SBL). The Geostrophic free-stream region is stably stratified and separated from the ABL by a capping inversion layer, which typically forms at a height around 1 km - 2 km (Stull, 1988; Liu and Liang, 2010). When a neutral ABL exists beneath the stably stratified inversion layer and the free-stream flow, a type of boundary layer called the Conventionally Neutral Boundary Layer (CNBL) is formed. The strength of the wind veer in the Ekman layer depends on the atmospheric thermal stability. In particular, the wind veer is most pronounced in an SBL, while a more substantial vertical mixing resulting from convection in the CBL leads to weaker wind veering (Deardorff, 1972; Wyngaard, 2010; Berg et al., 2013; Liu and Stevens, 2021).

Within the lower part of the ABL, the ASL, analytical expressions for the velocity profiles including the effects of thermal stratification, can be obtained using Monin-Obukhov Similarity Theory (MOST) (Monin and Obukhov, 1954; Dyer, 1974). MOST incorporates stability correction terms to account for the deviation from the logarithmic law behavior within the ASL due to the heating or cooling of the surface. Although the boundary layer region is neutrally stratified in CNBL flows, the stratification in the Geostrophic free-stream region influences the velocity profile in the surface layer. Studies such as Zilitinkevich et al. (2002), Taylor and Sarkar (2008), Abkar and Porté-Agel (2013), and Kelly et al. (2019) derived additional correction terms to the log law profile

122

123

125

126

127

128

129

130

131

133

134

135

137

138

141

142

143

144

145

147

148

149

150

151

152

153

154

155

156

157

158

159

161

162

163

165

that incorporate the effect of free-stream stratification. However, these corrections do not address the flow within the Ekman outer layer, where wind veering is significant. Gryning et al. (2007) used a mixing length approach to obtain the mean speed profile above the surface layer in cases including stratification. An additional layer was introduced where the mixing length decayed to zero around the ABL height. Moreover the friction velocity was assumed to decay linearly with height within the ABL. Although the velocity profiles were constructed to match the Geostrophic wind, the emphasis was on prediction of velocity magnitude within the first few hundred meters of the ABL and the model did not provide analytical predictions of the separate velocity components. In Kelly and Gryning (2010), the MOST and the Gryning model (Gryning et al., 2007) were extended to derive a long-term wind profile, using the probability distribution of the Obukhov length. Zilitinkevich and Esau (2005) also proposed analytical expressions for velocity components within the ASL based on an eddy-viscosity approach where ABL height and mixing lengths were modeled using an inverse interpolation function for different atmospheric conditions. The model constants pertaining to these interpolation functions were obtained using LES data. In this study, the effect of baroclinicity is also included by adding a linear baroclinic shear term to the wind shear. Recently, Ghannam and Bou-Zeid (2021) also derived an analytical model for the ABL velocity magnitude which captures the deviation of the velocity from the log law profile caused due to Baroclinic effects. We note that, in this study, we neglect baroclinic effects in the flow and focus on Geostrophic wind driven ABL flows.

Kadantsev et al. (2021) reformulated the Ekman mean momentum equations in terms of the turbulent stresses and derived analytical expressions for the stresses. The analytical velocity profiles were then obtained by integrating the model stresses divided by constant eddy-viscosity, which was modeled as the product of the friction velocity and a mixing length scale. Within the ASL, the mixing length was assumed to increase linearly with height until reaching a constant value in the Ekman layer. The constant value was determined based on an LES-tuned inverse quadratic expression for the turbulent length, which accounted for different atmospheric conditions. However, this assumption of a constant eddy-viscosity within the Ekman layer leads to inaccurate velocity predictions, particularly in the region approaching the top of the ABL.

In addition to modeling the shape of the velocity profile as a function of height, means to predict the friction velocity as a function of known Geostrophic velocity and surface roughness are also required. This is accomplished using what is often termed a Geostrophic Drag Law (GDL). Kadantsev et al. (2021) utilized LES to develop a GDL model capable of predicting Geostrophic wind and friction velocities across a range of stability conditions, including CNBL and SBL flows. In a recent study, Liu and Stevens (2022) proposed analytical expressions to predict both the streamwise and spanwise mean velocity components throughout the boundary layer height in CNBL flows. This study utilized a separate LES-based GDL model (Liu et al., 2021a) to obtain the magnitudes of the Geostrophic wind and friction velocity for different CNBL flow condi-

168

169

171

172

173

174

175

176

178

179

180

182

183

184

185

186

187

188

190

194

195

196

198

202

tions that are not directly based on the modeled velocity profile. Separately from their proposed GDL model, Liu and Stevens (2022) provided stability correction functions to predict the structure of the velocity components in the CNBL flows. Although its prediction of the vector velocity profile improves upon previous models that predicted CNBL wind speeds (Kelly et al., 2019; Liu et al., 2021b), the Liu and Stevens (2022) model was tailored to CNBL conditions. The extension of its applicability to SBL flows requires further development.

Motivated by the limitations of existing models, specifically the need for more efficient and accurate velocity predictions in CNBL and SBL flows, and a GDL that is self-consistently derived from the model of the velocity profile, we propose a two-layer approach. In an outer (Ekman) layer, we assume a self-similarity of turbulent stresses across stability conditions and a Nieuwstadt (1984) 3/2 power law profile. The second layer is an inner layer for the ASL that is consistent with the MOST description. Based on this description, we develop a self-consistent GDL to estimate the friction velocity and cross-isobaric angle by requiring continuity of mean velocities between the two layers. By incorporating the GDL into the model, we obtain the complete velocity profiles within the ABL for a variety of stability conditions (CNBL and a range of SBL). We validate our GDL and ABL wind model using data from the literature as well as from newly generated large-eddy simulations (LES). The proposed analytical velocity profile and GDL model are introduced in section §2. The LES datasets for model validation are described in section §3, while results and discussions are presented in section §4. Finally, overall conclusions are summarized in section §5.

2 Analytical model for ABL wind velocity profiles 191

We employ a Cartesian coordinate system, with the x, y, and z axes aligned with the streamwise (near the ground), spanwise, and wall-normal directions, respectively. Assuming a steady and horizontally homogeneous flow, we construct the model based on the streamwise and spanwise mean Ekman momentum equations (Ekman, 1905; Kadantsev et al., 2021):

$$0 = f_c[V(z) - V_g] + \frac{\partial T_{xz}(z)}{\partial z}, \tag{1}$$

$$0 = f_c[V(z) - V_g] + \frac{\partial T_{xz}(z)}{\partial z},$$

$$0 = -f_c[U(z) - U_g] + \frac{\partial T_{yz}(z)}{\partial z}.$$
(2)

In these equations, f_c represents the Coriolis frequency, while U(z) and V(z)correspond to the streamwise and spanwise components of the mean velocity, respectively. Additionally, $T_{xz}(z)$ and $T_{yz}(z)$ denote the turbulent stresses in 199 the streamwise and spanwise directions, respectively. For simplicity, we derive 200 the model assuming $f_c > 0$, which corresponds to the northern hemisphere. A simple change in the sign of the spanwise components of the velocity and

turbulent stress can be employed to model velocity profiles in the southern hemisphere.

The bottom boundary of the ABL is characterized by a surface roughness height z_0 , where the velocities adhere to the no-slip velocity condition, $U(z_0) = V(z_0) = 0$. In the region near the surface as z approaches z_0 , a constant flux zone exists, where the turbulent stresses are predominantly aligned in the streamwise direction at the surface. Since the streamwise direction near the surface is defined here as the x direction, $T_{xz}(z_0) = u_*^2$, where u_* is the friction velocity. Since $T_{yz}(z_0) = 0$, and the resultant total surface stress is $T(z_0) = \sqrt{T_{xz}^2(z_0) + T_{yz}^2(z_0)} = T_{xz}(z_0) = u_*^2$ (It is straightforward to recast any results in an arbitrarily chosen coordinate system, as long as the Geostrophic wind direction is adjusted accordingly).

The ABL extends to a height of h. Above h, the flow transitions into a region under Geostrophic balance, characterized by stable stratification and the absence of turbulent stresses. From (1) and (2), the velocity components in this Geostrophic region can be simplified to $V(z \ge h) = V_g$ and $U(z \ge h) = U_g$. Assuming a Geostrophic wind with a magnitude of G oriented at an angle α_0 relative to the streamwise (x) direction, the velocity components can be expressed as $U_g = G \cos \alpha_0$ and $V_g = G \sin \alpha_0$.

The dimensionless form of equations (1) and (2) utilize the friction velocity u_* and the Rossby-Montgomery length scale (Rossby and Montgomery, 1935) u_*/f_c as the characteristic velocity and length scales of the flow. The model to be developed in this paper is based on the dimensionless form of the mean momentum equations (1) and (2). For known values of U_g , V_g , u_* , and given the profiles of the non-dimensional form of turbulent stresses $\hat{T}_{xz}(\hat{\xi}) = T_{xz}(z)/u_*^2$, and $\hat{T}_{yz}(\hat{\xi}) = T_{yz}(z)/u_*^2$, we can obtain the ABL wind velocity profiles as:

$$\frac{V(z)}{u_*} = -\frac{\partial \hat{\mathbf{T}}_{xz}(\hat{\xi})}{\partial \hat{\xi}} + \frac{V_g}{u_*},\tag{3}$$

$$\frac{U(z)}{u_*} = \frac{\partial \hat{\mathbf{T}}_{yz}(\hat{\xi})}{\partial \hat{\xi}} + \frac{U_g}{u_*},\tag{4}$$

where $\hat{\xi} = z f_c/u_*$ represents the dimensionless vertical coordinate. Correspondingly, $\hat{h} = h f_c/u_*$ represents the dimensionless ABL height and $\hat{\xi}_0 = z_0 f_c/u_*$ defines the dimensionless surface roughness length.

In the following sections, we will describe the proposed model for the turbulent stresses ($\hat{\mathbf{T}}_{xz}$ and $\hat{\mathbf{T}}_{yz}$). This model will be used to self-consistently derive a new GDL to determine U_g , V_g , and u_* from the resulting velocity profiles. A classic form of the GDL to obtain the friction velocity and cross-isobaric angle for given Geostrophic velocity G and roughness length z_0 can be written as (Rossby and Montgomery, 1935; Tennekes and Lumley, 1972; Zilitinkevich and Esau, 2005; Liu et al., 2021a)

$$\frac{\kappa G \cos \alpha_0}{u_*} = \ln (Ro) - A,\tag{5}$$

$$\frac{\kappa G \sin \alpha_0}{u_*} = -B,\tag{6}$$

where $Ro = u_*/(f_c z_0)$ is the friction Rossby number, κ is the Von-Kármán constant (often taken to be $\kappa \approx 0.41$), and A, B are dimensionless parameters. Note that the resistive laws in equations (5),(6) are written here for the northern hemisphere, where $V_g < 0$. For the southern hemisphere, $V_g > 0$ which is prescribed by having a positive sign before the coefficient B in (6).

Previous studies have shown that the constants A and B depend on the atmosphere's stability conditions (Zilitinkevich and Esau, 2005; Kadantsev et al., 2021). In our current study, we develop new functional forms for the dimensionless constants A and B that can be used to self-consistently determine u_* and α_0 (and thus U_g and V_g) across neutral and stable atmospheric conditions.

2.1 Assumed turbulent stress distributions

Previous studies Nieuwstadt (1984), Zilitinkevich and Esau (2005), Liu et al. (2021b) have investigated the vertical profiles of the total stress \hat{T} within the CNBL and SBL flows. They proposed the following representation for the total stress $\hat{T} = \sqrt{\hat{T}_{xz}^2 + \hat{T}_{yz}^2}$:

$$\hat{T} = (1 - z/h)^{3/2} = (1 - \hat{\xi}/\hat{h})^{3/2}.$$
 (7)

Figure 1(a) confirms good agreement of this proposed self-similar profile with data from Large Eddy Simulations (LES) of CNBL and SBL flows (details about the LES are provided in §3). Here results for various stability conditions are plotted as solid lines in normalized form and the analytical Nieuwstadt (1984) model for total stress is denoted using yellow right-pointing triangle markers on a solid yellow line. (Relevant details about the data, and the u_* and h values used in the normalization are provided in section 3.2.) Figures 1(b,c) show results for the individual stress components, also showing reasonably good self-similar collapse in the ABL region when using the fitted boundary layer height \hat{h} to normalize the $\hat{\xi}$ axis. In order to develop an analytical expression for the velocity profiles from Eqs. (3) & (4), an additional model is needed for the spanwise turbulent stress component \hat{T}_{yz} . The streamwise one can then be obtained by ensuring the total stress is given by Eq. (7).

As discussed in the introduction, two distinct layers can be identified in the ABL: the outer or Ekman layer, and the inner or surface (ASL) layer. The outer layer is characterized by Coriolis effects and the gradual decay of turbulent stresses to zero as the ABL height h is approached. Motivated by the LES observations in Figure 1(b) we propose the following model of the spanwise turbulent stress in this outer region

$$\hat{T}_{yz}^{\text{outer}} = -g(\hat{\xi}) \left(1 - \hat{\xi}/\hat{h}\right)^{3/2}, \tag{8}$$

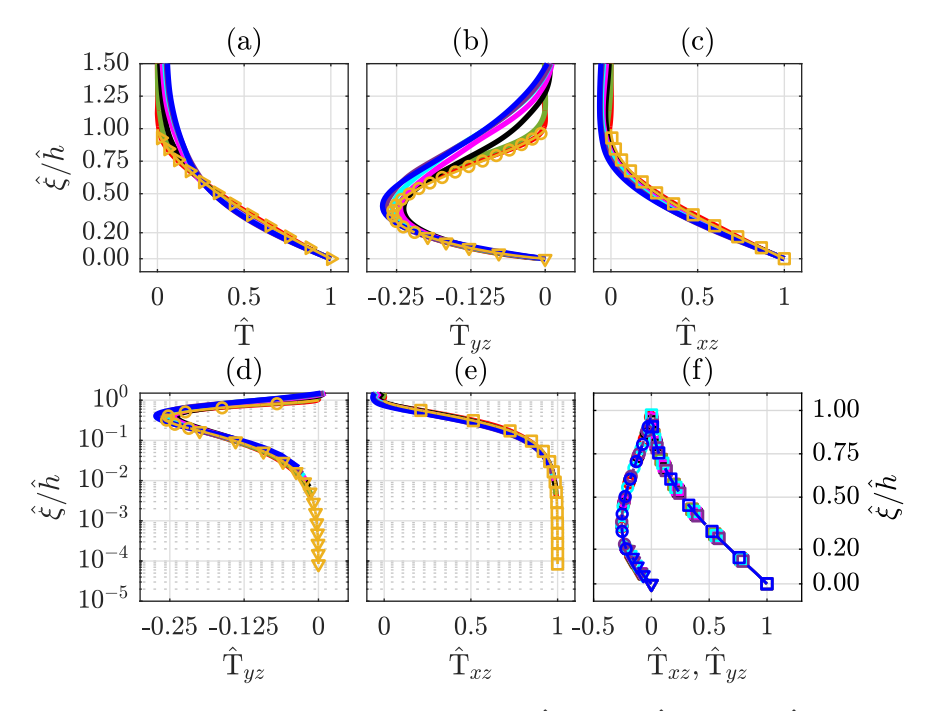


Fig. 1 Profiles of normalized turbulent stresses (a) \hat{T} , (b)&(d) \hat{T}_{yz} , (c)&(e) \hat{T}_{xz} from the LES (Table 2) of CNBL (—), SBL-1 (—), SBL-2 (—), SBL-3 (—), SBL-4 (—), SBL-5 (—), SBL-6 (—) compared with analytical profiles of \hat{T} (\rightarrow , Eq. 7), \hat{T}_{yz}^{outer} (\rightarrow , Eq. 8), \hat{T}_{yz}^{inner} (\rightarrow , Eq. 17), \hat{T}_{xz} (\rightarrow , Eq. 20) generated using the parameters of the CNBL case in Table 2. Plot (f) shows analytical profiles of \hat{T}_{xz} (\rightarrow , - \rightarrow , -

where,

$$g(\hat{\xi}) = c_g \left(1 - e^{-\hat{\xi}/\Gamma \hat{h}} \right). \tag{9}$$

It is constructed assuming $\hat{T}_{yz}^{\text{outer}}$ decays to zero both at the ABL height and at the surface, while aiming to preserve the 3/2 power law trend that is valid for the total stress magnitude over much of the domain. Closer to the surface, $g(\hat{\xi})$ becomes proportional to $\hat{\xi}$ and hence $\hat{T}_{yz}^{\text{outer}}$ vanishes at the surface as desired. An exponential form is chosen (instead of assuming that is simply linear in $\hat{\xi}$) in order to better match the data and ensure that the other component $\hat{T}_{xz}^{\text{outer}}$ (to be discussed later) remains realistic. In Eq. 9 $c_g=1.43$ is a fitting parameter obtained by calibrating the model with the results of the LES, see Figure 1(b). The constant c_g determines the magnitude of the turbulent spanwise stress and $\Gamma=0.83$ is chosen to reproduce the decay and diminishing contribution of the outer layer as $\hat{\xi}$ approaches $\hat{\xi}_0$ also ensuring that $g(\hat{\xi})<1$ as $\hat{\xi}$ approaches \hat{h} .

In addition, Eq. (9) effectively models the peak magnitude of the normalized spanwise shear stress, approximating it to be around 0.25—the mean value of the maximum magnitude of \hat{T}_{yz} observed in Figure 1(b) from LES. Similarly, the mean of the peak value of the dimensional (un-normalized) spanwise shear stress, $T_{yz}(z)$, from LES is 0.058. For \hat{T}_{yz} , the percentage difference relative to the mean value 0.25 remains consistently below 8% across the LES cases considered in this study, indicating a good collapse. In contrast, for the unnormalized stress $T_{yz}(z)$, the corresponding percentage differences relative to 0.058 as the mean value, reach as high as 50%. Modeling the normalized stress in the outer layer as a function independent of thermal stability conditions, offers a reliable representation of the observed behavior. The outer layer is assumed to be valid for $\hat{\xi} > \hat{\xi}_m$, i.e. above a certain transition height $\hat{\xi}_m$ to be specified later but that is typically expected to be 10-20% of the boundary layer height \hat{h} .

For $\xi \leq \xi_m$, the inner layer of the ABL consists of the log layer and the z-independent stratification layer (Zilitinkevich and Esau, 2005). Within this region, the wind veer is negligible, and the streamwise velocity for SBL (and CNBL) flows is governed by the Monin-Obukhov Similarity Theory (MOST) (Monin and Obukhov, 1954), which can be expressed as:

$$\frac{U^{\text{inner}}}{u_*} = \frac{1}{\kappa} \left(\ln \frac{z}{z_0} + 5 \frac{z - z_0}{L_s} \right). \tag{10}$$

Here L_s is the Obukhov length scale defined as

$$L_s = -\frac{u_*^3}{\kappa(g/\Theta_0)Q_0},\tag{11}$$

where Q_0 denotes the surface cooling flux and Θ_0 represents the reference potential temperature scale. Eq. (10) indicates that for the SBL flows, the velocity profile approximates the log layer very close to the ground since the log term becomes dominant as z approaches z_0 . Similarly, as we move further away from z_0 , the stability correction term becomes dominant. The ABL velocity follows the z-independent stratification behavior in which the velocity gradient is independent of z ($\partial U^{\text{inner}}/\partial z \approx 5u_*/\kappa L_s$) as the mixing length (ℓ) of the turbulent eddies is proportional to the Obukhov length. The pure logarithmic law for the truly neutral ABL (TNBL) flows without any thermal stratification effects is recovered for $1/L_s \to 0$. Using the dimensionless wall-normal distance $\hat{\xi} = zf_c/u_*$, Eq. (10) can be expressed as

$$\frac{U^{\text{inner}}}{u_*} = \frac{1}{\kappa} \ln \frac{\hat{\xi}}{\hat{\xi}_0} + 5\mu(\hat{\xi} - \hat{\xi}_0), \tag{12}$$

where μ is the Monin-Kazanski stability parameter (Arya, 1975; Smith, 1979; Tagliazucca and Nanni, 1983; Kitaigorodskii and Joffre, 1988) defined as

$$\mu = \frac{u_*}{\kappa f_c L_s}.\tag{13}$$

In the context of a CNBL flow, Kitaigorodskii and Joffre (1988) proposed that thermal stratification in the free stream Geostrophic region constrains the mixing length scale of turbulent eddies to u_*/N_{∞} , termed the Kitaigorodskii length scale. Here, $N_{\infty} = \sqrt{(g/\Theta_0)\gamma_{\Theta}}$ represents the Brunt-Väisälä frequency linked to the potential temperature with a lapse rate of γ_{Θ} (K/m) in the free stream region. Consequently, to characterize U^{inner} for both SBL and CNBL flows, we introduce a mixing length $\ell(z)$ defined by

$$\frac{1}{\ell(z)} = \frac{1}{\kappa z} + \frac{5}{\kappa L_s} + 0.3 \frac{N_{\infty}}{u_*}.$$
 (14)

In Eq. (14), the mixing length of the eddies exhibits a linear variation closer to the ground. However, far from the surface, the equation defines $\ell(z)$ in a way that physically limits the size of the eddies to the minimum value between L_s or u_*/N_{∞} . Similar formulations of $\ell(z)$ can be found in prior studies, including Zilitinkevich and Esau (2005), Gryning et al. (2007), and Kadantsev et al. (2021). While Gryning et al. (2007) employed a linear reciprocal-interpolation form similar to Eq. (14), Zilitinkevich and Esau (2005) and Kadantsev et al. (2021) utilized a quadratic form of the reciprocal interpolation $(1/\ell^2 = 1/(\kappa z)^2 + \cdots)$.

Assuming $\partial U^{\text{inner}}/\partial z \approx u_*/\ell(z)$ within the ASL, we incorporate Eq. (14) into this velocity gradient expression and integrate it vertically from z to z_0 , providing an analytical expression for U^{inner} applicable to both CNBL and SBL flows. Following normalization, the dimensionless model expression for U^{inner}/u_* is expressed as

$$\frac{U^{\text{inner}}}{u_*} = \frac{1}{\kappa} \ln \frac{\hat{\xi}}{\hat{\xi}_0} + (5\mu + 0.3\mu_N)(\hat{\xi} - \hat{\xi}_0), \tag{15}$$

where μ_N is the Zilitinkevich number defined as

$$\mu_N = \frac{N_\infty}{f_c}.\tag{16}$$

In strongly stably stratified ABL flows, we anticipate $1/L_s \gg 1/(u_*/N_\infty)$ $(\mu \gg \mu_N)$, leading to the recovery of the MOST expression for $U^{\rm inner}/u_*$ as given by Eq. (12). Conversely, as $1/L_s \to 0$ $(\mu = 0)$ in CNBL flows, we obtain $U^{\rm inner}/u_*$ with only the CNBL stability correction term, consistent with prior studies such as Taylor and Sarkar (2008); Abkar and Porté-Agel (2013). In Eq. (15), the model constant 0.3 in the CNBL correction term is obtained from the LES study conducted in Abkar and Porté-Agel (2013). We also note that Kelly et al. (2019) derived a different functional form of $U^{\rm inner}/u_*$ for CNBL flows using the Buckingham Pi theorem. This formulation was derived based on the vertical profiles of heat flux obtained from LES of CNBL flows, resulting in a quadratic expression for the stability correction term.

To determine associated inner layer stress, we substitute Eq. (15) into the y-momentum Eq. (4) and integrate along $\hat{\xi}$ to obtain the transverse stress

54 profile

357

358

359

360

361

364

365

366

368

369

370

371

372

373

375

376

377

378

379

380

381

382

383

385

$$\hat{T}_{yz}^{\text{inner}} = \frac{\hat{\xi}}{\kappa} \ln \frac{\hat{\xi}}{\hat{\xi}_0} - \frac{1}{\kappa} (\hat{\xi} - \hat{\xi}_0) \left[1 + \kappa \frac{U_g}{u_*} - \frac{\kappa}{2} (5\mu + 0.3\mu_N) (\hat{\xi} - \hat{\xi}_0) \right]. \tag{17}$$

Then combining equations (8) and (17), the spanwise turbulent stress \hat{T}_{yz} is modeled as:

$$\hat{T}_{yz} = \begin{cases} -g(\hat{\xi}) \left(1 - \frac{\hat{\xi}}{\hat{h}} \right)^{3/2} & \hat{\xi} > \hat{\xi}_m \\ \frac{\hat{\xi}}{\kappa} \ln \frac{\hat{\xi}}{\hat{\xi}_0} - (\hat{\xi} - \hat{\xi}_0) \left[\frac{1}{\kappa} + \frac{U_g}{u_*} - \frac{1}{2} (5\mu + 0.3\mu_N) (\hat{\xi} - \hat{\xi}_0) \right] & \hat{\xi} < \hat{\xi}_m \end{cases}$$
(18)

Note that in this equation, the value of U_g is not yet determined and will be found self-consistently later by enforcing continuity of velocities at the matching height $\hat{\xi}_m$. Based on LES results and consistent with usual expectations that the inner solution is valid in the lower 10-20% of the boundary layer height, we find that setting $\hat{\xi}_m = c_m \hat{h}$ with $c_m = 0.20$ leads to good results. The outer layer stress $\hat{T}_{yz}^{\text{outer}}$ from Eq. (8) and the inner layer stress $\hat{T}_{yz}^{\text{inner}}$ from Eq. (17) are plotted in Figure 1(b) using yellow circle and downward-pointing triangle markers on a solid yellow line, respectively. Both plots demonstrate good agreement with the LES data, though slight differences occur near the ABL height. While we assume $\hat{T}_{yz} = 0$ above the ABL height in the analytical model, Figure 1(b) shows stresses that are not zero in this region. The LES experiences an initial transient phase marked by the growth in turbulent boundary layer height, later quenched by the influence of stable stratification. This leads to a quasi-steady flow with stronger turbulence within the ABL, decaying to some non-zero residual stresses above the ABL height. Figures 1(d,e) use semilogarithmic axes to highlight the behavior of the inner portion near the ground.

In these comparisons, we have used the value of U_g/u_* determined from the proposed Geostrophic drag law (Eq. 5 with Eq. 33 to be developed in section §2.5). The model is evaluated for the same $z_0=0.1$ m as the LES and the cases shown correspond to $\mu=[0,5.62,20.59,39.84,59.25,78.35,148.49]$ and $\mu_N=61$ (see Table 2). Note that the analytical stress profiles in Figure 1(a)-(e) are plotted using the CNBL LES parameters $\mu=0$, and $\mu_N=61$. Figure 1(f) shows the analytical profiles of the turbulent stresses generated using all the LES parameters covering both the CNBL and SBL flows. We observe that these analytical turbulent stress components from the various LES cases lie on top of each other in Figure 1(f) with negligible differences occurring near the matching height $\hat{\xi}_m$. More detailed comparisons between the model and LES will be shown later in terms of velocity distributions.

393

394

395

The distribution of the normalized streamwise turbulent stress \hat{T}_{xz} is obtained directly from the definition of the total stress as follows:

$$\hat{T}_{xz} = \sqrt{\hat{T}^2 - \hat{T}_{yz}^2} \tag{19}$$

We can then use the model expressions for $\hat{\mathbf{T}}$ from Eq. (7), and $\hat{\mathbf{T}}_{yz}$ from Eq. (18) in (19) to obtain $\hat{\mathbf{T}}_{xz}$. For this component, an inner portion is not required: From Eq. (17), we observe that $\hat{\mathbf{T}}_{yz}^{\text{inner}}(\hat{\xi})$ tends to zero as $\hat{\xi}$ approaches $\hat{\xi}_0$. This shows that $\hat{\mathbf{T}}_{yz}^{\text{inner}} \ll \hat{\mathbf{T}}$ within the surface (inner) layer. In addition, since $\hat{\mathbf{T}}_{yz}^{\text{outer}}(\hat{\xi}_0) = 0$, we model $\hat{\mathbf{T}}_{xz}$ by using only $\hat{\mathbf{T}}_{yz}^{\text{outer}}$ in Eq. (19):

$$\hat{T}_{xz} = \sqrt{\hat{T}^2 - (\hat{T}_{yz}^{\text{outer}})^2} = \sqrt{1 - g(\hat{\xi})^2} \left(1 - \frac{\hat{\xi}}{\hat{h}}\right)^{3/2}.$$
 (20)

This analytical profile of \hat{T}_{xz} is plotted as yellow square markers on a yellow solid line in Figures $\mathbf{1}(c)\&(e)$, again showing good agreement with the LES. Using these turbulent stress models in the Ekman mean momentum equations, we obtain the ABL wind velocity profiles in the following section.

2.2 ABL velocity profiles

We obtain the analytical expressions for the ABL velocity profiles using the modeled stresses from (20) and (18) in (3) and (4), respectively and evaluating their derivatives analytically. The result is:

$$\frac{U(z)}{u_*} = \begin{cases}
-g'(\hat{\xi}) \left(1 - \frac{\hat{\xi}}{\hat{h}}\right)^{3/2} + g(\hat{\xi}) \frac{3}{2\hat{h}} \left(1 - \frac{\hat{\xi}}{\hat{h}}\right)^{1/2} + \frac{U_g}{u_*} &, \hat{\xi} \ge \hat{\xi}_m \\
\frac{1}{\kappa} \ln \frac{\hat{\xi}}{\hat{\xi}_0} + (5\mu + 0.3\mu_N)(\hat{\xi} - \hat{\xi}_0) &, \hat{\xi} \le \hat{\xi}_m
\end{cases} , (21)$$

$$\frac{V(z)}{u_*} = \frac{g(\hat{\xi})g'(\hat{\xi})}{\sqrt{1 - g(\hat{\xi})^2}} \left(1 - \frac{\hat{\xi}}{\hat{h}}\right)^{3/2} + \frac{3}{2\hat{h}}\sqrt{1 - g(\hat{\xi})^2} \left(1 - \frac{\hat{\xi}}{\hat{h}}\right)^{1/2} + \frac{V_g}{u_*}, \quad (22)$$

where $g'(\hat{\xi})$ is the derivative of $g(\hat{\xi})$

$$g'(\hat{\xi}) = \frac{c_g}{\Gamma \hat{h}} e^{-\hat{\xi}/\Gamma \hat{h}}.$$
 (23)

The streamwise velocity in (21) can be applied to both the northern and southern hemispheres. For the spanwise velocity in the southern hemisphere, a sign change is required for the first two terms on the right-hand side of (22). The sign of the Geostrophic velocity component V_g is set by the GDL Eq. (6).

In summary, note that the approach followed here is based on the empirical observation that fitting the scaled stress profiles based on the Nieuwstadt 3/2 profile (in outer region), seems relatively easier than fitting the velocities given the more complex shape of these profiles. In the inner (MOST) part, where we know how to model the profiles ($\sim \log x$), it is trivial to find the stress trends ($\sim x \log x + ...$) that give that inner velocity. We merge the two stress parts together and then take derivatives to find the velocity self-consistently. (As an aside, we note that recently Kelly and van der Laan (2023) derived analytical expressions linking directional shear to the shear and the vertical gradient of cross-wind stress components, for arbitrary stress profiles.)

In order for the model equations (21) and (22) to be complete, we still need to specify the ABL height \hat{h} , friction velocity u_* , Geostrophic velocity components U_g/u_* and V_g/u_* , and stability parameter μ . The latter requires L_s , which needs specification of the surface cooling flux Q_0 .

2.3 Model for surface cooling flux

408

411

412

413

415

416

417

418

419

424

427

In this section, we aim to relate Q_0 to the imposed cooling rate $C_r = \partial \Theta_s / \partial t$ of the surface potential temperature (Θ_s) . The governing equation for the evolution of the mean potential temperature (Θ) for the SBL flows is given by

$$\frac{\partial \Theta}{\partial t} = -\frac{\partial \langle w'\theta' \rangle}{\partial z},\tag{24}$$

where $\langle w'\theta' \rangle$ represents the turbulent heat flux.

When the SBL reaches a quasi-stationary state, the difference between the potential temperature within the boundary layer and the surface temperature, $\Theta(t) - \Theta_s(t)$ is steady (Wyngaard, 1975; Brost and Wyngaard, 1978). Using this quasi-steady assumption, Eq. (24) can be written as

$$\frac{\partial}{\partial t}(\Theta - \Theta_s) + \frac{\partial \Theta_s}{\partial t} = -\frac{\partial \langle w'\theta' \rangle}{\partial z}, \implies \frac{\partial \langle w'\theta' \rangle}{\partial z} = -C_r. \tag{25}$$

Integrating Eq. (25) across the SBL height assuming $h \gg z_0$, we get an analytical estimate for the surface cooling flux Q_0 :

$$\int_{z_0}^h \frac{\partial \langle w'\theta' \rangle}{\partial z} dz = -\int_{z_0}^h C_r dz, \implies Q_0 \equiv \langle w'\theta' \rangle_s = C_r h.$$
 (26)

In obtaining Eq. (26), we have used $\langle w'\theta'\rangle_h = 0$, the top boundary condition for the heat flux. Also, note that we are assuming that the height for the heat flux profile is the same as that for the momentum fluxes. This assumption may not be exactly correct, but it appears to be a reasonable approximation and is consistent with prior studies Wyngaard (1975); Brost and Wyngaard (1978).

Using (26) in (11), the Monin-Obukhov length scale L_s for the SBL flows can be expressed as

$$L_s = \frac{u_*^3 \Theta_0}{\kappa a \left(-C_r\right) h}. (27)$$

As a result, we model the Monin-Kazanski stability parameter μ (Eq. 13) as follows:

$$\mu = \frac{u_*}{\kappa f_c L_s} = \frac{g(-C_r)}{u_* f_c^2 \Theta_0} \frac{h f_c}{u_*} = \frac{g(-C_r)}{u_* f_c^2 \Theta_0} \hat{h}.$$
 (28)

In our current study, we perform the LES of SBL flows using cooling rates $C_r = [0, -0.03, -0.125, -0.25, -0.375, -0.5, -1]$ K/hr (see Table 2). The corresponding stability parameter μ ranges between 0 to 148.49. The comparison of the model estimates for Q_0 (26) and stability parameter μ (28) with the LES values are discussed in detail in section §4.1. This expression to calculate μ is used in the evaluation of the entire velocity profile U(z) from Eq. (21) (it does not directly affect the profile V(z) although indirectly it affects the profile via its dependence on u_* , which is affected by the value of μ).

The model expressions for μ and velocity profiles depend on the non-dimensional ABL height \hat{h} . In the following section, we discuss the model expression for determining the ABL height for a given atmospheric stability condition.

452 2.4 ABL height model

We utilize a well-established equilibrium ABL height model, which has been extensively studied in previous works such as Zilitinkevich et al. (2007) and Liu et al. (2021a), to determine the non-dimensional ABL height. This model is expressed as follows:

$$\frac{1}{\hat{h}^2} = \frac{1}{C_{TN}^2} + \frac{\mu_N}{C_{CN}^2} + \frac{\mu}{C_{NS}^2},\tag{29}$$

where μ is the stability parameter and μ_N is the Zilitinkevich number given by equations (13) and (16), respectively.

This expression represents a smooth merging of dimensionless height models corresponding separately to the TNBL, CNBL, and SBL flows. Liu et al. (2021a) performed a suite of LES of the CNBL flows and obtained $C_{TN}=0.5$ and $C_{CN}=1.6$ by fitting to LES data, and we adopt those values as well. Similarly, we determine the model parameter $C_{NS}=0.78$ via fitting results from the LES of the SBL flows performed as part of our current study. The LES data used to obtain the model constants are discussed in Section 3.

Incorporating the model for μ from Eq. (28), we can re-write the expression for \hat{h} as

$$\frac{1}{\hat{h}^3} = \frac{1}{\hat{h}} \left[\frac{1}{C_{TN}^2} + \frac{\mu_N}{C_{CN}^2} \right] + \frac{1}{C_{NS}^2} \frac{g(-C_r)}{u_* f_c^2 \Theta_0}.$$
 (30)

Using Eq. (30) with these empirically determined model parameters along with specifying the parameters μ_N and C_r , we can compute the non-dimensional ABL height \hat{h} spanning different conventionally neutral and stable atmospheric stability conditions. The cubic Eq. (30) can be solved e.g., iteratively (more details provided below). However, it is evident from Eq. (30) that we also require knowledge of the friction velocity u_* . We estimate u_* from the new Geostrophic drag law model discussed in the following section.

2.5 New Geostrophic Drag Law

468

470

473

474

487

488

490

Completing the analytical model requires a method to determine u_* and the flow angle α_0 for given flow conditions and surface roughness z_0 . We follow the classical approach of matching the inner (MOST) solution to outer conditions. In our context, we match the streamwise velocity profiles in Eq. (21) at the matching height $\hat{\xi}_m = c_m \hat{h}$, which enables us to determine U_g/u_* as follows:

$$\frac{U_g}{u_*} = \frac{1}{\kappa} \ln \frac{c_m \hat{h}}{\hat{\xi}_0} + (5\mu + 0.3\mu_N)(c_m \hat{h} - \hat{\xi}_0)
+ g'(\hat{\xi}_m) [1 - c_m]^{3/2} - g(\hat{\xi}_m) \frac{3}{2\hat{h}} \sqrt{1 - c_m}.$$
(31)

For V(z) no inner layer was required and thus the matching can be done by evaluating the spanwise velocity at the surface roughness height $\hat{\xi} = \hat{\xi}_0$. The result is

$$\frac{V_g}{u_*} = -\frac{3}{2\hat{h}}.\tag{32}$$

Since $U_g = G \cos \alpha_0$ and $V_g = G \sin \alpha_0$, comparing equations (31) and (32) with the classical GDL expressions from Eqs. (5) and (6) for the northern hemisphere we get the following new expressions for the coefficients A and B:

$$A = -\ln c_m \hat{h} - \kappa \left[(5\mu + 0.3\mu_N)(c_m \hat{h} - \hat{\xi}_0) + g'(\hat{\xi}_m) (1 - c_m)^{3/2} - g(\hat{\xi}_m) \frac{3}{2\hat{h}} \sqrt{1 - c_m} \right],$$
(33)

$$B = \frac{3\kappa}{2\hat{h}}. (34)$$

The equations (5), (6), (33), (34) together constitute the new Geostrophic drag law model. Note that the coefficients A and B depend on \hat{h} and the stability parameters, μ_N , and μ . Similar dependence of B on \hat{h} were discussed in previous studies such as Liu et al. (2021a), Ghannam and Bou-Zeid (2021),

Kadantsev et al. (2021). The presence of these stability parameters allows for the estimation of u_* and α_0 for both the CNBL and SBL flows. However, obtaining these estimates is challenging due to the non-linear and interdependent nature of the GDL equations when coupled with the model expressions for \hat{h} Eq. (30) and $\mu = g(-C_r)\hat{h}/(u_*f_c^2\Theta_0)$ Eq. (28). As a result, obtaining entirely closed-form analytical solutions is not possible. One must solve the set of equations numerically and we propose a simple iterative approach to obtain h, u_*, α_0 .

We implement this iterative solution using a two-step process. Starting from an initial guess for h and u_* , we first solve for h and u_* from the ABL height model Eq. (30) and the GDL equations Eqs. (5), (6), (33), (34). Eliminating α_0 from the GDL equations, one obtains (Tennekes and Lumley, 1972):

$$u_* = \frac{\kappa G}{\sqrt{[\ln(Ro) - A]^2 + B^2}}.$$
 (35)

Here A and B are from Eqs. (33), (34). The model for μ from Eq. (28) is also utilized by the expression for A. We obtain dimensional values of h, u_* by iteratively solving equations (30) and (35).

From the dimensional estimates of h, u_* found in the previous step, we can evaluate $\hat{h} = hf_c/u_*$, $\hat{\xi}_0 = z_0f_c/u_*$ and $\mu = g(-C_r)\hat{h}/(u_*f_c^2\Theta_0)$. Using these results, we can obtain the GDL coefficients A and B. Given these coefficients, we evaluate U_g and V_g from Eqs. (5) and (6), respectively. Finally, from the Geostrophic velocities, we find the cross-isobaric angle using $\alpha_0 = \tan^{-1}(V_g/U_g)$. This iterative process of evaluating h, u_*, α_0 is explained in more detail in Appendix A.

3 Description of Large Eddy Simulation data for model validation

Large Eddy Simulations have played a major role in improving our understanding of the ABL under various stability conditions (Saiki et al., 2000; Beare et al., 2006; Kumar et al., 2006). This section describes the various LES datasets used to validate our analytical model. Prior LES-based research has investigated several parameterizations of resistive laws and wind profiles for a CNBL flow, see e.g., Abkar and Porté-Agel (2013), Liu et al. (2021a), Liu et al. (2021b), and Liu and Stevens (2022). We describe the CNBL data from this existing literature in section §3.1. We perform additional LES runs including SBL flows in this study, which we describe in section §3.2. We utilize the ABL height (h), friction velocity (u_*) , and cross-isobaric angle (α_0°) values obtained in the prior studies and these new LES to validate our GDL model.

3.1 LES data of CNBL flows from existing literature

In these previous studies, the LES of the CNBL was set with a linear initial potential temperature profile, given by $\Theta(z) = \Theta_0 + \gamma_{\Theta} z$. Here, γ_{Θ} represents the

lapse rate of potential temperature in the free-stream Geostrophic region, and Θ_0 is a reference potential temperature. For the initial velocity profiles, Abkar and Porté-Agel (2013) employed a laminar flow with random perturbations added near the surface within the first 100 m to initiate turbulence. Similarly, Liu et al. (2021a), Liu et al. (2021b), and Liu and Stevens (2022) utilized a uniform velocity profile with a Geostrophic wind magnitude G, along with random perturbations within the first 100 m from the surface. By imposing a thermally insulating boundary condition at the bottom wall, a quasi-steady CNBL flow is established, characterized by a mean potential temperature exhibiting a capping inversion layer that separates the neutral boundary layer region from the Geostrophic free-stream region. In these earlier studies, the height of the CNBL (h) was determined using a criterion where h corresponds to the height at which the total shear stress decreases to 5% of the wall stress.

In Abkar and Porté-Agel (2013), the CNBL flow was examined with a Geostrophic wind magnitude of G=10 m/s. Two surface roughness heights, namely $z_0=0.01$ m and $z_0=0.1$ m, were considered while the Coriolis frequency was fixed to $f_c=10^{-4}$ 1/s. Two free-stream stratification strengths were chosen to yield Zilitinkevich numbers of $\mu_N=58$ and $\mu_N=180$. A total of four LES cases were performed in that study. The specific values for the CNBL height, friction velocity, and cross-isobaric angle corresponding to these cases are listed in Table 1. The study's findings demonstrated that, for a given surface roughness height, an increase in the stratification strength of the free stream resulted in a reduction in the height of the CNBL. Conversely, for a fixed free-stream stratification strength, an increase in the surface roughness height led to an increase in the CNBL height.

In Liu et al. (2021a), the LES of CNBL flows were studied with a Geostrophic wind of magnitude G = 12 m/s. In their study, the surface roughness height was fixed to $z_0 = 10^{-4}$ m while the Coriolis frequencies were varied representing the ABL flows in low and high-latitude regions. Three free-stream stratification strengths were considered such that the parameter μ_N ranged between 42 to 1350. In summary, Liu et al. (2021a) performed twenty-four LES simulations of the CNBL flow. Table 1 lists the values of the non-dimensional numbers μ_N , Ro and the dimensional estimates of h, u_*, α_0 for these twentyfour cases. Liu et al. (2021a) revisited the GDL model proposed in Zilitinkevich and Esau (2005) and provided updated model coefficients for predicting u_*, α_0 for the CNBL flows. Consistent with the findings of Abkar and Porté-Agel (2013), their results demonstrated that for a given surface roughness height, the CNBL depth gets shallower as the free stream stratification strength is increased. Liu et al. (2021a) also showed that the CNBL height becomes smaller in high latitude regions characterized by an increase in the magnitude of the Coriolis frequency.

For our model validation, we also consider another six sets of LES performed in Liu et al. (2021b) and Liu and Stevens (2022). These studies performed the LES to predict the structure of the CNBL flows driven by a Geostrophic wind of magnitude G=12 m/s. Liu et al. (2021b) proposed an analytical model for the resultant wind velocity profile while in Liu and

Stevens (2022), both the streamwise and spanwise components of the velocity profiles were obtained. Although the dimensional values of h, u_*, α_0 for these cases are not explicitly reported in the references, we estimate these quantities using the GDL model described in Liu and Stevens (2022) for the given values of μ_N and Ro. The corresponding values of μ_N , Ro, u_* , h and α_0 for these six simulations are listed in Table 1.

Description	μ_N	Ro	h(m)	$u_*(m/s)$	$\alpha_0(^\circ)$
	-		, ,	, , ,	
Data 1	58	4.33×10^{4}	793	0.4332	18.49
	58	3.61×10^{5}	661	0.3606	14.88
	180	4.11×10^{4}	433	0.4105	27.75
	180	3.48×10^5	375	0.3477	23
D + 0	40	0.0 107	400	0.0004	11.00
Data 2	42	2.3×10^7	482	0.3084	11.88
	72	2.3×10^7	396	0.3084	13.02
	125	2.3×10^{7}	312	0.3096	14.98
	45	2.4×10^{7}	507	0.3072	11.93
	78	2.4×10^{7}	413	0.3072	13.12
	136	2.4×10^{7}	326	0.3072	15.16
	51	2.8×10^{7}	552	0.3048	11.92
	89	2.8×10^{7}	438	0.3048	13.45
	154	2.8×10^{7}	350	0.3048	15.41
	61	3.3×10^{7}	602	0.3024	12.13
	106	3.3×10^{7}	477	0.3036	13.79
	183	3.3×10^{7}	375	0.3024	16.20
	78	4.0×10^{7}	692	0.2988	12.46
	136	4.0×10^{7}	533	0.3000	14.64
	235	4.0×10^{7}	417	0.2988	17.38
	115	5.9×10^{7}	835	0.2940	13.31
	199	5.9×10^{7}	636	0.2928	16.02
	344	5.7×10^7	485	0.2868	19.26
	226	1.1×10^8	1109	0.2820	16.12
	391	1.1×10^{8}	826	0.2736	20.02
	678	1.0×10^{8}	613	0.2604	24.88
	557	1.5×10^{8}	942	0.2628	22.89
	965	1.4×10^{8}	698	0.2472	28.02
	1350	1.8×10^8	778	0.2328	31.31
D + 0	F1.0	2.70 107	F 70	0.0105	11.00
Data 3	51.2	2.70×10^7	573	0.3135	11.96
	88.7	4.50×10^4	744	0.5166	22.26
	88.7	3.70×10^5	616	0.4278	18.28
	88.7	3.20×10^6	522	0.3626	15.42
	88.7	2.70×10^{7}	453	0.3147	13.34

$$153.6 \quad 2.70 \times 10^7 \quad 351 \quad 0.3135 \quad 15.67$$

Table 1: Table lists the CNBL LES data from Abkar and Porté-Agel (2013) (Data 1), Liu et al. (2021a) (Data 2), Liu et al. (2021b) (Data 3).

3.2 Additional LES data including SBL flows

The LES data in Table 1 consists only of CNBL cases. We perform additional LES simulations including SBL flows. We use the LESGO solver that has seen many applications for ABL simulations (Albertson and Parlange, 1999; Bou-Zeid et al., 2005; Kumar et al., 2006; Sescu and Meneveau, 2015; Calaf et al., 2010; Stevens et al., 2014b,a; Sescu and Meneveau, 2014; Abkar et al., 2018; Shapiro et al., 2020).

We discuss the governing equations and numerical methodology of the LESGO solver in Section 3.2.1. We then present the simulation setup in Section 3.2.2.

590 3.2.1 Governing equations and numerical method

LESGO solves the filtered Navier-Stokes equations with a buoyancy force term approximated using the Boussinesq approximation and the scalar potential temperature transport equation:

$$\frac{\partial \tilde{u}_{i}}{\partial x_{i}} = 0,$$

$$\frac{\partial \tilde{u}_{i}}{\partial t} + \tilde{u}_{j} \left(\frac{\partial \tilde{u}_{i}}{\partial x_{j}} - \frac{\partial \tilde{u}_{j}}{\partial x_{i}} \right) = -\frac{1}{\rho_{0}} \frac{\partial p_{\infty}}{\partial x_{i}} - \frac{\partial \tilde{p}}{\partial x_{i}} + \frac{g}{\tilde{\theta}_{0}} (\tilde{\theta} - \tilde{\theta}_{0}) \delta_{i3} - \frac{\partial \tau_{ij}}{\partial x_{j}} - f_{c}\tilde{u} \delta_{i2} + f_{c}\tilde{v} \delta_{i1},$$

$$\frac{\partial \tilde{\theta}}{\partial t} + \tilde{u}_{j} \frac{\partial \tilde{\theta}}{\partial x_{i}} = -\frac{\partial \Pi_{j}}{\partial x_{i}},$$
(38)

where the tilde $(\tilde{\cdot})$ represents a spatial filtering operation such that $\tilde{u}_i = (\tilde{u}, \tilde{v}, \tilde{w})$ are the filtered velocity components in the streamwise, lateral and vertical directions, respectively, and $\tilde{\theta}$ is the filtered potential temperature. The term $\tau_{ij} = \sigma_{ij} - (1/3)\sigma_{kk}\delta_{ij}$ is the deviatoric part of the Sub-Grid Scale (SGS) stress tensor $\sigma_{ij} = \tilde{u}_i \tilde{u}_j - \tilde{u}_i \tilde{u}_j$. The quantity $\tilde{p} = \tilde{p}_*/\rho_0 + (1/3)\sigma_{kk} + (1/2)\tilde{u}_j \tilde{u}_j$ is the modified pressure, where the actual pressure \tilde{p}_* divided by the ambient density ρ_0 is augmented with the trace of the SGS stress tensor and the kinematic pressure arising from writing the non-linear terms in rotational form. The δ_{ij} in the momentum Eq. (37) is the Kronecker delta function determining the direction of the buoyancy and Coriolis forces. In the buoyancy term, $g = 9.81 \text{ m/s}^2$ is the gravitational acceleration, $\tilde{\theta}_0$ is the reference potential

temperature scale. The Coriolis frequency in the Coriolis force term is defined as $f_c = 2\Omega \sin \phi$, where ϕ is the latitude angle of a given region. In the potential temperature Eq. (38), the term $\Pi_j = u_j \theta - \tilde{u}_j \tilde{\theta}$ is the SGS heat flux. The SGS terms τ_{ij} and Π_j are modeled as

$$\tau_{ij} = -2\nu_T^{\text{SGS}}\tilde{S}_{ij}, \qquad \Pi_i = -\kappa_T^{\text{SGS}}\partial\tilde{\theta}/\partial x_i, \qquad (39)$$

where $\tilde{S}_{ij} = (1/2)(\partial \tilde{u}_i/\partial x_j + \partial \tilde{u}_j/\partial x_i)$ is the symmetric part of the velocity gradient tensor, ν_T^{SGS} and κ_T^{SGS} are the SGS momentum and heat diffusivities, respectively. The SGS Prandtl number (Pr_{SGS}) relates the two diffusivities, which are evaluated as

$$\nu_T^{\text{SGS}} = (C_s \tilde{\Delta})^2 \sqrt{\tilde{S}_{ij} \tilde{S}_{ij}}, \qquad \kappa_T^{\text{SGS}} = P r_{\text{SGS}}^{-1} \nu_T^{SGS}.$$
 (40)

Here, C_s is the Smagorinsky model coefficient, and $\tilde{\Delta} = (\Delta x \Delta y \Delta z)^{1/3}$ is the effective grid spacing or filter width. The model coefficient C_s is evaluated using the Lagrangian dynamic scale-dependent model (Bou-Zeid et al., 2005).

To represent an ABL that is driven by a Geostrophic wind, we apply a mean pressure gradient $-(1/\rho_0)\partial p_{\infty}/\partial x_i$ in Eq. (37), which is determined from the Geostrophic balance:

$$\rho_0^{-1} \partial p_\infty / \partial x = f_c V_g, \quad \rho_0^{-1} \partial p_\infty / \partial y = -f_c U_g. \tag{41}$$

Here, we set the Geostrophic wind magnitude $G = \sqrt{U_g^2 + V_g^2}$ while the direction of the wind α (such that $U_g = G\cos\alpha$, $V_g = G\sin\alpha$) is controlled by a Proportional-Integral (PI) controller designed to impose a desired mean velocity orientation at a particular height (Sescu and Meneveau, 2014; Narasimhan et al., 2022). For future wind energy applications, we selected that the mean velocity is aligned in the streamwise direction at a height of 100 m, but simulation results are rotated in order to obtain zero spanwise mean velocity at the ground after the simulation is completed to be consistent with the model formulation.

The code employs a pseudo-spectral technique to discretize the streamwise and spanwise directions. For discretizing the wall-normal direction, a second-order central finite difference method is utilized. To advance in time, the code employs the second-order accurate Adams-Bashforth scheme. In order to reduce the effects of streamwise periodicity, a shifted periodic boundary condition is employed (Munters et al., 2016).

The effect of atmospheric stability is incorporated in the boundary condition by evaluating the surface momentum fluxes utilizing the MOST expression for the mean velocity. Assuming the first grid point is within the ASL region, the corresponding surface momentum flux τ_w is given by

$$\tau_w = -\left(\frac{\tilde{u}_r \kappa}{\ln(z_1/z_0) - \Psi_{\rm m}(z_1/L_s) + \Psi_{\rm m}(z_0/L_s)}\right)^2,\tag{42}$$

where $\tilde{u}_r = \sqrt{\tilde{u}^2 + \tilde{v}^2}$ is the resultant horizontal velocity at the first grid point $z = z_1 = \Delta z/2$, $\kappa = 0.41$ is the Von Karman constant, and z_0 is the surface roughness height, while L_s is the Monin-Obukhov length. From Eq. (42), the surface momentum flux components are evaluated as:

$$\tau_{i,3|w} = \tau_w \times (\tilde{u}_i/\tilde{u}_r), \ i = 1, 2.$$
 (43)

These are applied as a boundary condition at the bottom boundary, while a stress-free boundary condition is imposed on the top boundary.

The L_s in Eq. (42) is evaluated in LES as follows

$$L_s = u_*^2 \tilde{\theta}_1 / (\kappa g T_*), \tag{44}$$

where the friction velocity is evaluated as $u_* = \sqrt{|\tau_w|}$, $\tilde{\theta}_1$ is the potential temperature at the first grid point and $T_* = -Q_0/u_*$ is a temperature scale that represents the ratio of the surface heat flux and the friction velocity. For the SBL flows, $Q_0 < 0$ and correspondingly $T_* > 0$ resulting in $L_s > 0$. The model for the potential temperature provides T_* according to

$$T_* = -\frac{Q_0}{u_*} = \frac{\kappa[\tilde{\theta}_1 - \tilde{\theta}_s]}{\ln(z_1/z_{0s}) - \Psi_h(z_1/L_s) + \Psi_h(z_{0s}/L_s)}.$$
 (45)

Here $\tilde{\theta}_s$ is the surface potential temperature and z_{0s} is the surface roughness height for the potential temperature which is taken to be $z_{0s} = 0.1z_0$ (Brutsaert, 2005). To simulate an SBL flow, we decrease the surface temperature by specifying a constant cooling rate C_r ($C_r < 0$). We use this C_r to evaluate $\tilde{\theta}_s(t)$ at a given time step using $\tilde{\theta}_s(t) = \tilde{\theta}_s(t - \Delta t) + C_r \Delta t$.

The stability functions $\Psi_{\rm m}(\zeta=z/L_s)$ and $\Psi_{\rm h}(\zeta=z/L_s)$ in equations (42) and (45), respectively, are obtained from Chenge and Brutsaert (2005) given by

$$\Psi_{\rm m/h}(\zeta = z/L_s) = -a_{\rm m/h} \ln \left[\zeta + (1 + \zeta^{b_{\rm m/h}})^{b_{\rm m/h}^{-1}} \right],$$
 (46)

where the constants are $a_{\rm m} = 6.1, b_{\rm m} = 2.5, a_{\rm h} = 5.3, b_{\rm h} = 1.1.$

In order to dampen the gravity waves in the computational domain, a sponge (or Rayleigh damping) layer is used at the top boundary. This is a wave-absorbing layer spanning 500 meters from the top boundary. Within this layer, a body force with a cosine profile for its damping coefficient is employed to mitigate the reflection of gravity waves. (Allaerts and Meyers, 2017; Durran and Klemp, 1983).

3.2.2 Simulation setup

644

646

649

650

652

653

654

655

657

658

661

662

663

The LES for the current study is performed in a computational domain of size $L_x \times L_y \times L_z = 3.75$ km \times 1.5 km \times 2 km. The streamwise, spanwise, and wall-normal directions are discretized using $N_x \times N_y \times N_z = 360 \times 144 \times 432$ grid points. The resulting grid resolution is $\Delta x \times \Delta y \times \Delta z = 10.4$ m $\times 4.6$ m. We set the Geostrophic wind magnitude as G = 15 m/s, Coriolis

frequency $f_c=10^{-4}~{\rm s}^{-1}$, surface roughness height $z_0=0.1$ m, SGS Prandtl number $Pr^{\rm SGS}=1$. According to Basu and Lacser (2017), for MOST-based wall-modeled LES studies, it is recommended to employ a criterion where the initial point on the grid is at a distance of at least $50z_0$ from the surface. Accordingly, for $z_0=0.1$ m, we opt for $\Delta z\approx 5$ m in this study. In addition, Gadde and Stevens (2021) found that the turbulence statistics of SBL flows remain invariant when altering the streamwise domain size or horizontal grid resolution. They employed a 9 m grid resolution in the horizontal direction. In our study, we adopt a comparable grid resolution.

For both the CNBL and SBL simulations, the velocity fields are initialized with a log-law velocity profile superimposed with a zero-mean white noise within the first 100 m from the surface to initiate turbulence. A description of the respective setups of the initial potential temperature profile for the CNBL and SBL simulations is as follows.

We first perform the LES of a CNBL flow using an initial linear potential temperature profile $\Theta(z) = \Theta_0 + \gamma_\Theta z$ with $\Theta_0 = 265$ K, and $\gamma_\Theta = 0.001$ K/m. The simulation reaches a quasi-stationary state where the boundary layer height grows to 1157 m. The resulting temperature profile has a capping inversion layer at the ABL height which separates the neutral boundary layer region from the stably stratified Geostrophic region. Under quasi-steady conditions, the potential temperature within the CNBL region stayed around 265.58 K.

For the LES of SBL flows, we initialize potential temperature using the CNBL's quasi-steady potential temperature profile. We then decrease the magnitude of the surface potential temperature $\hat{\theta}_s$ by applying different cooling rates $C_r = [-0.03, -0.125, -0.25, -0.375, -0.5, -1]$ K/hr to induce stable stratification. The simulations are run until reaching a quasi-steady state. We then perform time and planar averaging to obtain the vertical profiles of the turbulent stresses and mean wind velocities. Time averaging is done over a 10–12 hour window, which we observe to be long enough for the flow to be quasi-steady with no appreciable effects from inertial oscillations. The dimensional ABL height h is determined by a least-square-error minimization method for the root mean square difference between the normalized LES stress $\hat{T} = T(z)/u_*^2$ and the model expression $(1-z/h)^{3/2}$, in a range between 0 < z < h. The resultant values of h, u_*, α_0 are listed in Table 2. Since the PI controller maintains a streamwise aligned mean flow at z = 100 m, the α_0 values reported in Table 2 are obtained by geometrically rotating the mean velocity profiles such that wind veer is zero at the first grid point. This is done to be consistent with the GDL model derivation using a coordinate system in which there is no wind veer within the ASL region.

Case	μ	Ro	C_r (K/hr)	h (m)	u_* (m/s)	$lpha_0^\circ$
CNBL	0	6.02×10^4	0	1157	0.60	21

SBL-1 SBL-2 SBL-3 SBL-4 SBL-5	5.62 20.59 39.84 59.25 78.35	5.93×10^4 5.25×10^4 4.58×10^4 4.12×10^4 3.84×10^4	-0.03 -0.125 -0.25 -0.375 -0.5	1032 662 463 361 306	0.59 0.53 0.46 0.41 0.38	24 28 32 35 38
SBL-5 SBL-6	148.49	3.84×10^{4} 3.39×10^{4}	-0.5 -1	218	0.38 0.34	38 41

Table 2: Description of LES of CNBL and SBL cases with corresponding values of stability parameter μ , friction Rossby number Ro, Cooling rate C_r (K/hr), ABL height h (m), friction velocity u_* (m/s), and cross-isobaric angle α_0° . For all simulations, G=15 m/s, $z_0=0.1$ m, $\Theta_0=265$ K. The Coriolis frequency is $f_c=10^{-4}$ s⁻¹ and the free-stream Brunt-Väisälä frequency is $N_{\infty}=6.1\times10^{-3}$ s⁻¹ which gives the Zilitinkevich number $\mu_N=61$.

In the following section, we use these forty-one LES cases covering a range of atmospheric conditions for validation of the comprehensive ABL wind model discussed in section §2.

⁷¹⁴ 4 Results and discussion

In this section, we validate the ABL wind model by comparing the model predictions with the corresponding LES cases. We first compare our new GDL approach in section §4.1. We then compare the ABL wind velocity profile predictions with the LES in section §4.2.

4.1 GDL: LES vs Model

We determined the ABL height h, friction velocity u_* , and the cross-isobaric angle α_0 from the new GDL model described in §2 using the iterative procedure described in the Appendix A. For each of the forty-one LES cases described in §3, we use the inputs $(G, z_0, f_c, C_r, N_\infty)$ that are known from the LES and predict the unknown values h, u_* , and α_0 using the new GDL model.

The GDL model predictions are compared with the LES in Figures 2(a), (b), and (c). The colored markers represent the forty-one LES cases. The markers (\triangleright) and (\triangleleft) represent the CNBL and SBL cases, respectively, from the LES cases in Table 2 while the rest of the markers represent the CNBL data from previous studies (Table 1). The GDL predictions for h, u_*, α_0 lie close to the solid black line signifying excellent agreement with the LES. By choosing the matching height at $\hat{\xi}_m = 0.2\hat{h}$, the relative root mean square error between the GDL model predictions and LES for h, u_*, α_0 is found to be 7%. We consider this percentage error to be well within acceptable limits

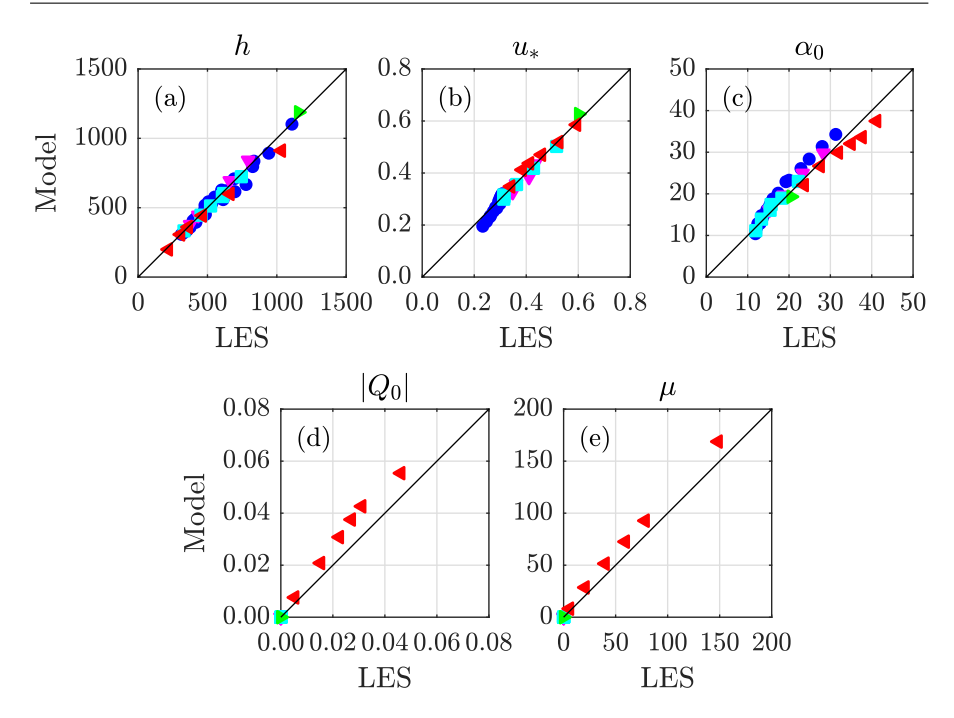


Fig. 2 GDL predictions of (a) ABL height h (in meters), (b) friction velocity u_* (m/s), (c) cross-isobaric angle α_0 (in degrees), (d) surface cooling flux magnitude $Q_0 = C_r h$ (Eq. 26) in (K m/s), (e) stability parameter μ (Eq. 28) compared against the LES of CNBL cases from Liu et al. (2021a) (\bullet), Abkar and Porté-Agel (2013) (\blacktriangledown), Liu and Stevens (2022) (\blacksquare), CNBL LES (\blacktriangleright) & LES of SBL (\blacktriangleleft) from current work.

demonstrating good agreement of the model with the data. In addition, the maximum absolute differences between model vs LES for $U_g = G\cos\alpha_0$ and $V_g = G\sin\alpha_0$ are 0.64 m/s and 0.87 m/s. We consider these differences to be within agreeable limits as well. The comparison of the model estimates for the surface cooling flux $Q_0 = C_r h$ (Eq. 26) and the stability parameter μ (Eq. 28) are shown in Figure 2(d) and (e). While $Q_0 = \mu = 0$ for the CNBL cases, the non-zero values corresponding to the SBL cases show good agreement with the LES. The slight discrepancies observed between the model predictions for Q_0 and μ compared to LES are attributed to variations in the heights at which momentum and scalar heat fluxes decay to zero.

These results suggest that the newly proposed GDL formulation is able to predict ABL height h, friction velocity u_* , and cross-isobaric angle α_0 correctly for the different flow and thermal stability conditions for the data in Tables 1 and 2.

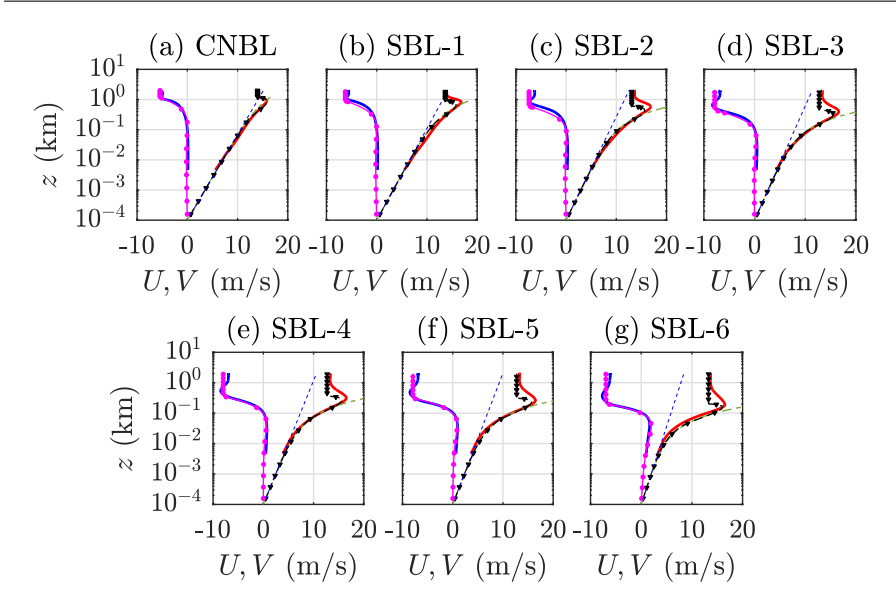


Fig. 3 Plot comparing model predictions of U(z) ($- \mathbf{v}$ -, Eq. 21) and V(z) ($- \mathbf{v}$ -, Eq. 22) with the log-law profile $(\kappa^{-1}u_* \ln[z/z_0] - \cdots)$, the MOST model ($- \cdot \cdot \cdot$, Eq. 15), and LES $(U(z) - \cdots, V(z) - \cdots)$ from (a) CNBL, (b) SBL-1, (c) SBL-2, (d) SBL-3, (e) SBL-4, (f) SBL-5, (g) SBL-6. The vertical z-axis is presented in a semi-logarithmic scale.

4.2 Velocity profiles: LES vs Model

750

751

752

753

754

755

756

757

758

759

760

761

762

763

764

765

766

767

769

In this section, we compare the ABL wind velocity profiles from the model with the LES for the cases described in Table 2. We show the comparison of the vertical variation of the streamwise and spanwise velocity components in Figures 3(a)-(g) and Figures 4(a)-(h). The plots in Figure 3 use a logarithmic scale for the vertical direction while for Figure 4, the vertical axis is scaled in linear units. Plots 3(a) and 4(a) correspond to the CNBL case while the Figures 3 & 4 (b)-(g) are from the SBL cases where the cooling rate is progressively increased from -0.03 K/hr to -1 K/hr. The solid red and blue lines in these plots are U(z) and V(z) profiles from the LES, respectively. The black dashed lines with a triangle marker and magenta lines with circle marker are the model predictions from Eq. (21) and Eq. (22), respectively. The blue dashed line in Figure 3 represents the log-law profile. The green dash-dotted line in both figures represent the MOST prediction including the CNBL correction given by Eq. (15). Both Figures 3 and 4 are plotted by applying the model with zero veer at 100 m height, as in the LES. The semi-logarithmic plot in Figures 3(a)-(g) clearly show that V(z = 100 m) = 0. The horizontal line just above the origin in Figures 4(a)-(h) also represents this 100 m height where we see that V(z = 100 m) = 0 in all these figures.

In Figure 3, all the streamwise velocity curves follow the log law close to the ground within the constant flux region of the ASL. Upon increasing the cooling rate, the stable stratification causes deviation of the velocity profile

from the log law behavior. This stability-affected region is in the z-independent stratification layer as it matches the shape from the MOST with the CNBL correction. The wind veer is also negligible within the ASL. Above the ASL lies the Ekman layer, where the wind veer is stronger, and the MOST predictions deviate significantly from the LES and also do not satisfy the Geostrophic condition. Whereas the ABL wind model Eq. (21) for U(z) captures the low-level jet profile for different stability conditions where it reaches a peak velocity at some height and then decreases to the Geostrophic wind velocity at the ABL height as shown in Figures 3 and 4. Most importantly, the model also predicts the wind veer profiles from Eq. (22) while theories like the MOST do not model the wind direction.

The wind veer velocity profiles within the ABL region for all the cases are plotted together in Figure 4(h). The plot clearly shows the effect of increasing the cooling rate. Under strong stable stratification, the SBL height decreases, and the wind veer strength is intensified closer to the ground causing a significant cross-wind flow. The ABL wind model is able to capture the decrease in the ABL height as well as the intense wind veer profiles. Another important aspect of the model is the accurate prediction of u_* and Geostrophic velocities U_g, V_g from the self-consistent GDL model. The flow velocity in the Geostrophic region is set to these predicted values of U_g and V_g , again in good agreement with the LES asymptotically far above z = h.

The analytical velocity profiles from Eqs. (21) & (22) show good overall agreement with the LES for most of the domain. More specifically, the CNBL prediction is in excellent agreement with the LES, while deviations exist for the SBL cases near the ABL height where the model assumes a sharp change in slope while the LES profile is more smeared out. We attribute the larger discrepancies near at ABL height to non-zero turbulent stresses above the SBL region. In developing the analytical model, we assumed the turbulent stresses were zero above the ABL height. However, from the LES, we see non-zero residual stresses exist above the boundary layer (See Fig. 1(b).) which we have explained in detail under section 2.1.

In summary, the above comparisons demonstrate the capability of the new ABL wind model. The model can successfully predict the ABL wind velocity profiles for the entire domain across both conventionally neutral and stable atmospheric conditions. These analytical predictions can be used as an input in Gaussian models for modeling wind turbine wakes (Bastankhah and Porté-Agel, 2014) or pollution puffs (Zannetti, 1990) in the ABL.

5 Conclusions

In this study, we developed an analytical model to predict the steady-state mean velocity profiles for thermally stratified and conventionally neutral ABL flows. We showed the turbulent stress components are approximately self-similar for the CNBL and SBL flows. We directly model these turbulent stresses using analytical formulations representing the self-similarity in the

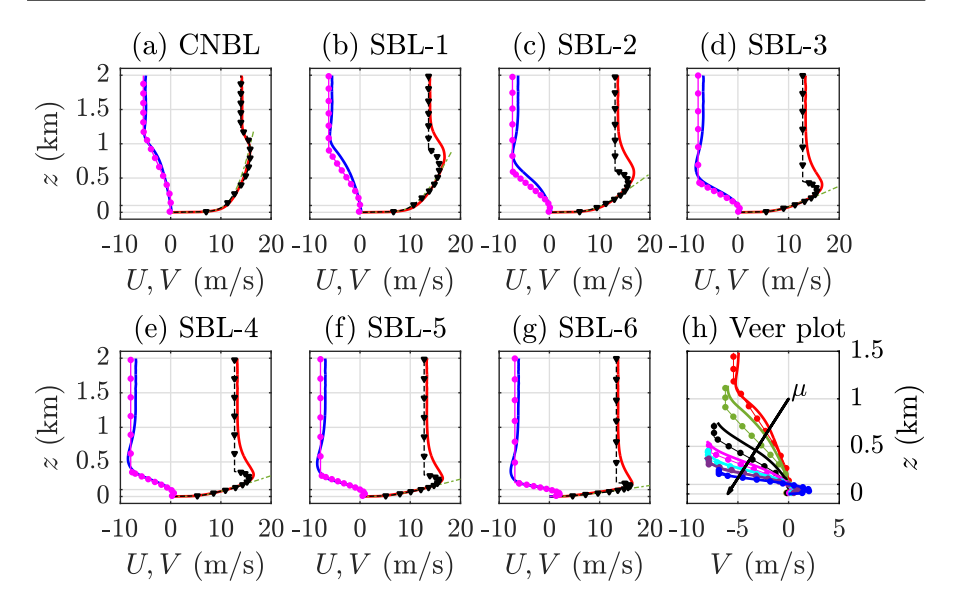


Fig. 4 Model predictions of U(z) ($\neg \nabla \neg$, Eq. 21) and V(z) ($\multimap \neg$, Eq. 22) compared against the MOST model ($\neg \neg \neg$, Eq. 15) and LES ($U(z) \neg \neg \neg$, $V(z) \neg \neg \neg$) from (a) CNBL, (b) SBL-1, (c) SBL-2, (d) SBL-3, (e) SBL-4, (f) SBL-5, (g) SBL-6. The veer plot in (h) shows how stronger stable stratification (increasing μ) causes a decrease in the ABL height, resulting in a strong wind veer flow. Figure (h) consists of the analytical wind veer estimates that are represented by a circle marker on a thin solid line and different colors represent CNBL ($\multimap \neg$), SBL-1 ($\multimap \neg$), SBL-2 ($\multimap \neg$), SBL-3 ($\multimap \neg$), SBL-4 ($\multimap \neg$), SBL-5 ($\multimap \neg$), SBL-6 ($\multimap \neg$). The corresponding LES estimates of V(z) in (h) are plotted as solid lines without the circle marker using the same color as analytical estimates.

stresses using Nieuwstadt (1984)'s 3/2 power law, and an inner layer consistent with MOST-based modeling. These stress profiles were incorporated into the Ekman mean momentum equations to predict the ABL velocity components. Furthermore, we derived a self-consistent Geostrophic drag law model by matching the streamwise velocity in the inner and outer layer regions at a specific height and evaluating the spanwise velocity at the surface roughness height. We used an LES-based equilibrium ABL height model which predicts the ABL height for the different types of boundary layer spanning neutral and stable boundary layer flows.

The effects of thermal stratification are characterized by the stability parameters μ_N and μ which influenced the model expressions for turbulent stresses, velocity components, and the GDL. We assumed the parameter Zilitinkevich number μ_N is known and modeled the stability parameter μ by representing the surface cooling flux as the product of the cooling rate and ABL height. We used this modeled μ in the analytical expressions for the velocities, turbulent stresses, and the GDL.

To validate our model, we compared our predictions with corresponding values obtained from LES from literature and new cases run specifically for SBL flows, and demonstrated a good agreement between them. The new model

can predict ABL mean velocity profiles under different atmospheric stability conditions, showing maximum absolute differences of 2 m/s within the ABL and Geostrophic regions, and 4 m/s around the ABL height when compared to LES data. In conclusion, the new analytical model provides reliable predictions of ABL velocity profiles, capturing the MOST velocity profiles within the surface layer and the Ekman spiral structure within the Ekman layer, which eventually merges with the Geostrophic wind above the ABL.

Future work aims to extend the approach to also describe convective boundary layers and perhaps allow to capture unsteady effects such as during a daily cycle. Development of further model refinements including other effects such as momentum exchanges due to canopies (Patton et al., 2016) or wind farms (Calaf et al., 2010) is also of significant interest.

Acknowledgements: This research has received support from the National Science Foundation (NSF) through grants CBET-1949778 and CMMI-2034111. We extend our gratitude for the high-performance computing (HPC) assistance received from Cheyenne (doi:10.5065/D6RX99HX), made available by NCAR's CISL and sponsored by the NSF. Additionally, the work has benefited from resources offered by the Advanced Research Computing at Hopkins (ARCH) core facility (rockfish.jhu.edu), backed by the NSF under grant OAC1920103.).

Appendix A: Summary of ABL model and iterative solution method 853

In this Appendix section, we summarize the iterative method to solve the coupled equations 854 for the proposed ABL model discussed in section §2. 855

- 1. Input values: N_{∞} , f_c , G, z_0 , C_r (assuming $f_c > 0$, northern hemisphere).
- 857

858 859

860

861

862

863

864

866

869

- Input values, $v_{\infty}, j_c, \sigma_1, \sigma_0$; (as Assume initial values for h^0, u_*^0 and set $h^n = h^0, u_*^n = u_*^0$. (b) Compute u_*^{n+1} using Eq. (35):

$$u_*^{n+1} = \frac{\kappa G}{\sqrt{[\ln{(Ro^n)} - A^n]^2 + (B^n)^2}}, \text{ where}$$
 (47)

$$A^{n} = -\ln c_{m} \hat{h}^{n} - \kappa \left[(5\mu^{n} + 0.3\mu_{N})(c_{m} \hat{h}^{n} - \hat{\xi}_{0}^{n}) + g'(c_{m} \hat{h}^{n})(1 - c_{m})^{3/2} - g(c_{m} \hat{h}^{n}) \frac{3}{2\hat{h}^{n}} \sqrt{1 - c_{m}} \right],$$

$$B^{n} = \frac{3\kappa}{2\hat{h}^{n}}, \text{ and}$$

 $g(c_m \hat{h}^n) = c_g \left[1 - e^{-c_m/\Gamma} \right], \ g'(c_m \hat{h}^n) = \frac{c_g}{\Gamma \hat{h}^n} e^{-c_m/\Gamma}, \ c_g = 1.43, \ \Gamma = 0.83,$ $\mu^n = \frac{g\left(-C_r\right)}{u_*^n f_c^2 \, \Theta_0} \hat{h}^n, \quad \hat{\xi}_0 = \frac{z_0 f_c}{u_*^n}, \quad \hat{h}^n = \frac{h^n f_c}{u_*^n}, \ c_m = 0.20.$

(c) Compute h^{n+1} using u_*^{n+1} from Eq. (47) in Eq. (30):

$$h^{n+1} = \frac{u_*^{n+1}}{f_c} \left[\frac{1}{C_{TN}^2} + \frac{\mu_N}{C_{CN}^2} + \frac{1}{C_{NS}^2} \frac{(g/\theta_0)(-C_r)h^n}{u_*^{n+1}^2 f_c} \right]^{-1/2},$$

 $C_{TN} = 0.5, \ C_{CN} = 1.6, \ C_{NS} = 0.78, \ \mu_N = N_{\infty}/f_c$

- (d) Iterate till convergence to get final values of u_*, h .
- Then evaluate:

$$\hat{h} = \frac{hf_c}{u_*}, \ \hat{\xi}_0 = \frac{z_0f_c}{u_*}, \ \mu = \frac{g\left(-C_r\right)}{u_*f_c^2\,\Theta_0}\hat{h}, \ Ro = \frac{u_*}{z_0f_c},$$

865

as well as the converged values of A and B. 4. Evaluate U_g,V_g using the GDL equations (Eqs. 5, 6, 33, 34):

$$U_g = \frac{u_*}{\kappa} \left(\ln \left(Ro \right) - A \right), \quad V_g = -\frac{u_*}{\kappa} B,$$

and obtain $\alpha_0 = \tan^{-1}\left(\frac{V_g}{U_g}\right)$. 5. Evaluate U(z) and V(z) with $\hat{\xi} = zf_c/u_*$: 867

$$U(z) = \begin{cases} u_* \left(-g'(\hat{\xi}) \left[1 - \frac{\hat{\xi}}{\hat{h}} \right]^{3/2} + g(\hat{\xi}) \frac{3}{2\hat{h}} \sqrt{1 - \frac{\hat{\xi}}{\hat{h}}} \right) + U_g &, \ \hat{\xi} \ge \hat{\xi}_m \\ u_* \left(\frac{1}{\kappa} \ln \frac{\hat{\xi}}{\hat{\xi}_0} + (5\mu + 0.3\mu_N)(\hat{\xi} - \hat{\xi}_0) \right) &, \ \hat{\xi} \le \hat{\xi}_m \end{cases}$$

$$V(z) = u_* \left(\frac{g(\hat{\xi})g'(\hat{\xi})}{\sqrt{1 - g(\hat{\xi})^2}} \left[1 - \frac{\hat{\xi}}{\hat{h}} \right]^{3/2} + \frac{3}{2\hat{h}} \sqrt{1 - g(\hat{\xi})^2} \left[1 - \frac{\hat{\xi}}{\hat{h}} \right]^{1/2} \right) + V_g.$$

877

878

882

883

886

887

888

891

892

894

895

896

898

899

900

906

907

908

909

910

912

914

915

References

- Abkar M, Porté-Agel F (2013) The effect of free-atmosphere stratification on boundary-871 layer flow and power output from very large wind farms. Energies 6(5):2338-2361, DOI 872 10.3390/en6052338 873
- Abkar M, Sørensen JN, Porté-Agel F (2018) An analytical model for the effect of vertical 874 wind veer on wind turbine wakes. Energies 11(7), DOI 10.3390/en11071838 875
 - Albertson JD, Parlange MB (1999) Surface length scales and shear stress: Implications for land-atmosphere interaction over complex terrain. Water Resources Research 35(7):2121-2132, DOI 10.1029/1999WR900094
- Allaerts D, Meyers J (2017) Boundary-layer development and gravity waves in conventionally 879 neutral wind farms. Journal of Fluid Mechanics 814:95-130, DOI 10.1017/ifm.2017.11 880
 - Arya SPS (1975) Geostrophic drag and heat transfer relations for the atmospheric boundary layer. Quarterly Journal of the Royal Meteorological Society 101(427):147-161, DOI https://doi.org/10.1002/qj.49710142712
- Bastankhah M, Porté-Agel F (2014) A new analytical model for wind-turbine wakes. Re-884 newable Energy 70:116–123, DOI https://doi.org/10.1016/j.renene.2014.01.002 885
 - Basu S, Lacser A (2017) A cautionary note on the use of monin-obukhov similarity theory in very high-resolution large-eddy simulations. Boundary-Layer Meteorology 163(2):351-355, DOI 10.1007/s10546-016-0225-y
- Beare R, Macvean M, Holtslag A, Cuxart J, Esau I, Golaz J, Jimenez M, Khairoutdinov M, Kosovic B, Lewellen D, et al. (2006) An intercomparison of large-eddy simulations of the 890 stable boundary layer. Boundary-Layer Meteorology 118:247–272
- Berg J, Mann J, Patton EG (2013) Lidar-observed stress vectors and veer in the atmospheric boundary layer. Journal of Atmospheric and Oceanic Technology 30(9):1961 – 1969, DOI 893 https://doi.org/10.1175/JTECH-D-12-00266.1
 - Blackadar AK (1962) The vertical distribution of wind and turbulent exchange in a neutral atmosphere. Journal of Geophysical Research (1896-1977) 67(8):3095-3102, DOI https: //doi.org/10.1029/JZ067i008p03095
 - Bou-Zeid E, Meneveau C, Parlange M (2005) A scale-dependent Lagrangian dynamic model for Large Eddy Simulation of complex turbulent flows. Physics of Fluids 17(2):025,105, DOI 10.1063/1.1839152
- Brost RA, Wyngaard JC (1978) A model study of the stably stratified planetary boundary 901 layer. Journal of Atmospheric Sciences 35(8):1427 - 1440, DOI 10.1175/1520-0469(1978) 902 $035\langle 1427:AMSOTS\rangle 2.0.CO; 2$ 903
- Brutsaert W (2005) Hydrology: An Introduction. Cambridge University Press, DOI 10.1017/ 904 CBO9780511808470
 - Calaf M, Meneveau C, Meyers J (2010) Large Eddy Simulation study of fully developed windturbine array boundary layers, Physics of Fluids 22(1):015.110, DOI 10.1063/1.3291077
 - Chenge Y, Brutsaert W (2005) Flux-profile relationships for wind speed and temperature in the stable atmospheric boundary layer. Boundary-Layer Meteorology 114(3):519-538, DOI 10.1007/s10546-004-1425-4
 - Constantin A, Johnson RS (2019) Atmospheric Ekman flows with variable eddy viscosity. Boundary-Layer Meteorology 170(3):395-414, DOI 10.1007/s10546-018-0404-0
 - Deardorff JW (1972) Numerical investigation of neutral and unstable planetary boundary layers. Journal of Atmospheric Sciences 29(1):91 - 115, DOI https://doi.org/10.1175/ 1520-0469(1972)029(0091:NIONAU)2.0.CO;2
- Durran DR, Klemp JB (1983) A compressible model for the simulation of moist moun-916 tain waves. Monthly Weather Review 111(12):2341 - 2361, DOI 10.1175/1520-0493(1983) 917 111(2341:ACMFTS)2.0.CO;2 918
- Dyer AJ (1974) A review of flux-profile relationships. Boundary-Layer Meteorology 7(3):363-372, DOI 10.1007/BF00240838 920
- Ekman VW (1905) On the influence of the earth's rotation on ocean-currents. Arkiv For 921 Matematik, Astronimi och Fysik 922
- Ellison TH (1955) The Ekman spiral. Quarterly Journal of the Royal Meteorological Society 923 81(350):637-638, DOI https://doi.org/10.1002/qj.49708135025

947

948 949

955

957

964

965 966

- Gadde SN. Stevens RJAM (2021) Interaction between low-level iets and wind farms in a sta-925 ble atmospheric boundary layer. Phys Rev Fluids 6:014,603, DOI 10.1103/PhysRevFluids. 926 6.014603 927
- Ghannam K, Bou-Zeid E (2021) Baroclinicity and directional shear explain departures from the logarithmic wind profile. Quarterly Journal of the Royal Meteorological Society 929 147(734):443-464, DOI https://doi.org/10.1002/qj.3927 930
- Gryning SE, Batchvarova E, Brümmer B, Jørgensen H, Larsen S (2007) On the extension of 931 the wind profile over homogeneous terrain beyond the surface boundary layer. Boundary-932 Layer Meteorology 124(2):251-268, DOI 10.1007/s10546-007-9166-9 933
- Horst TW (1997) A simple formula for attenuation of eddy fluxes measured with first-934 order-response scalar sensors. Boundary-Layer Meteorology 82(2):219-233, DOI 10.1023/ 935 A:1000229130034
- Kadantsev E, Mortikov E, Zilitinkevich S (2021) The resistance law for stably stratified 937 atmospheric planetary boundary layers. Quarterly Journal of the Royal Meteorological 938 Society 147(737):2233-2243, DOI 10.1002/qj.4019 939
- Kelly M, Gryning SE (2010) Long-term mean wind profiles based on similarity theory. 940 Boundary-Layer Meteorology 136(3):377–390, DOI 10.1007/s10546-010-9509-9 941
- 942 Kelly M, van der Laan MP (2023) From shear to veer: theory, statistics, and practical application. Wind Energy Science 8(6):975-998, DOI 10.5194/wes-8-975-2023 943
- Kelly M, Cersosimo RA, Berg J (2019) A universal wind profile for the inversion-capped neutral atmospheric boundary layer. Quarterly Journal of the Royal Meteorological Society 945 145(720):982-992, DOI https://doi.org/10.1002/qj.3472 946
 - Kitaigorodskii SA, Joffre SM (1988) In search of a simple scaling for the height of the stratified atmospheric boundary layer. Tellus A: Dynamic Meteorology and Oceanography 40(5):419–433, DOI 10.3402/tellusa.v40i5.11812
- Krishna K (1980) The planetary-boundary-layer model of Ellison (1956)—a retrospect. 950 Boundary-Layer Meteorology 19(3):293-301, DOI 10.1007/BF00120593 951
- Kumar V, Kleissl J, Meneveau C, Parlange MB (2006) Large-eddy simulation of a diurnal cycle of the atmospheric boundary layer: Atmospheric stability and scaling issues. Water 953 resources research 42(6) 954
- Liu L, Stevens RJAM (2021) Effects of atmospheric stability on the performance of a wind turbine located behind a three-dimensional hill. Renewable Energy 175:926-935, DOI 956 https://doi.org/10.1016/j.renene.2021.05.035
- Liu L, Stevens RJAM (2022) Vertical structure of conventionally neutral atmospheric bound-958 ary layers. Proceedings of the National Academy of Sciences 119(22):e2119369,119, DOI 959 10.1073/pnas.2119369119
- Liu L, Gadde SN, Stevens RJAM (2021a) Geostrophic drag law for conventionally neutral 961 atmospheric boundary layers revisited. Q J R Meteorol Soc 147(735):847-857, DOI https: 962 //doi.org/10.1002/qj.3949 963
 - Liu L, Gadde SN, Stevens RJAM (2021b) Universal wind profile for conventionally neutral atmospheric boundary layers. Phys Rev Lett 126:104,502, DOI 10.1103/PhysRevLett. 126.104502
- Liu S, Liang XZ (2010) Observed diurnal cycle climatology of planetary boundary 967 layer height. Journal of Climate 23(21):5790 - 5809, DOI https://doi.org/10.1175/ 2010JCLI3552.1 969
- Monin A, Obukhov AM (1954) Basic laws of turbulent mixing in the surface layer of the 970
- Munters W, Meneveau C, Meyers J (2016) Shifted periodic boundary conditions for 972 simulations of wall-bounded turbulent flows. Physics of Fluids 28(2):025,112, DOI 973 10.1063/1.4941912
- Narasimhan G, Gayme DF, Meneveau C (2022) Effects of wind veer on a yawed wind 975 turbine wake in atmospheric boundary layer flow. Phys Rev Fluids 7:114,609, DOI 10. 976 1103/PhysRevFluids.7.114609 977
- Nieuwstadt FTM (1984) The turbulent structure of the stable, nocturnal boundary layer. 978 Journal of Atmospheric Sciences 41(14):2202 - 2216, DOI https://doi.org/10.1175/ $1520-0469(1984)041\langle 2202:TTSOTS\rangle 2.0.CO; 2$ 980
- Patton E, Sullivan P, Shaw R, Finnigan J, Weil J (2016) Atmospheric stability influences 981 on coupled boundary layer and canopy turbulence. Journal of the Atmospheric Sciences

```
73(4):1621-1647
```

- Rossby CG, Montgomery RB (1935) The layer of frictional influence in wind and ocean currents. vol 3, pp 1–101, DOI 10.1575/1912/1157
- Saiki E, Moeng C, Sullivan P (2000) Large-eddy simulation of the stably stratified planetary boundary layer. Boundary-Layer Meteorology 95:1–30
- Sescu A, Meneveau C (2014) A control algorithm for statistically stationary Large Eddy Simulations of thermally stratified boundary layers. Q J R Meteorol Soc 140(683):2017–2022, DOI https://doi.org/10.1002/qj.2266
- Sescu A, Meneveau C (2015) Large-eddy simulation and single-column modeling of thermally stratified wind turbine arrays for fully developed, stationary atmospheric conditions. Journal of Atmospheric and Oceanic Technology 32(6):1144-1162
 - Shapiro CR, Gayme DF, Meneveau C (2020) Generation and decay of counter-rotating vortices downstream of yawed wind turbines in the atmospheric boundary layer. Journal of Fluid Mechanics 903:R2, DOI DOI:10.1017/jfm.2020.717
 - Smith F (1979) The relation between pasquill stability p and kazanski-monin stability μ (in neutral and unstable conditions). Atmospheric Environment (1967) 13(6):879–881, DOI https://doi.org/10.1016/0004-6981(79)90279-8
 - Stevens RJAM, Gayme DF, Meneveau C (2014a) Large Eddy Simulation studies of the effects of alignment and wind farm length. Journal of Renewable and Sustainable Energy 6(2):023,105, DOI 10.1063/1.4869568
 - Stevens RJAM, Graham J, Meneveau C (2014b) A concurrent precursor inflow method for Large Eddy Simulations and applications to finite length wind farms. Renewable Energy 68:46–50, DOI https://doi.org/10.1016/j.renene.2014.01.024
 - Stull RB (1988) An Introduction to Boundary Layer Meteorology, 1st edn. Springer Netherlands, DOI 10.1007/978-94-009-3027-8
 - Tagliazucca M, Nanni T (1983) An atmospheric diffusion classification scheme based on the kazanski-monin stability parameter. Atmospheric Environment (1967) 17(11):2205–2211, DOI https://doi.org/10.1016/0004-6981(83)90217-2
- Taylor JR, Sarkar S (2008) Stratification effects in a bottom ekman layer. Journal of Physical Oceanography 38(11):2535 2555, DOI https://doi.org/10.1175/2008JPO3942.1
 - Tennekes H, Lumley JL (1972) A First Course in Turbulence. The MIT Press, DOI 10.7551/mitpress/3014.001.0001
- Walcek CJ (2002) Effects of wind shear on pollution dispersion. Atmospheric Environment
 36(3):511-517, DOI https://doi.org/10.1016/S1352-2310(01)00383-1
 - Wyngaard JC (1975) Modeling the planetary boundary layer —extension to the stable case. Boundary-Layer Meteorology 9(4):441–460, DOI 10.1007/BF00223393
 - Wyngaard JC (2010) Turbulence in the Atmosphere. Cambridge University Press, DOI 10.1017/CBO9780511840524
 - Zannetti P (1990) Gaussian Models, Springer US, Boston, MA, pp 141–183. DOI 10.1007/978-1-4757-4465-1_7
 - Zilitinkevich S, Esau I (2005) Resistance and heat-transfer laws for stable and neutral planetary boundary layers: Old theory advanced and re-evaluated. Q J R Meteorol Soc 131:1863 1892, DOI 10.1256/qi.04.143
 - Zilitinkevich S, Esau I, Baklanov A (2007) Further comments on the equilibrium height of neutral and stable planetary boundary layers. Q J R Meteorol Soc 133(622):265–271, DOI https://doi.org/10.1002/qj.27
- Zilitinkevich SS, Perov VL, King JC (2002) Near-surface turbulent fluxes in stable stratification: Calculation techniques for use in general-circulation models. Quarterly Journal of the Royal Meteorological Society 128(583):1571–1587, DOI https://doi.org/10.1002/qj.200212858309